# Trapping Oxygen in Hierarchically Porous Carbon Nano-nets: Graphitic Nitrogen Dopants Boost the Electrocatalytic Activity

Li-Na Han, Xiao Wei, Bing Zhang, Xin-Hao Li*, Qian-Cheng Zhu, Kai-Xue Wang, and Jie-Sheng Chen*

School of Chemistry and Chemical Engineering, Shanghai Jiao Tong University, Shanghai 200240, P. R. China

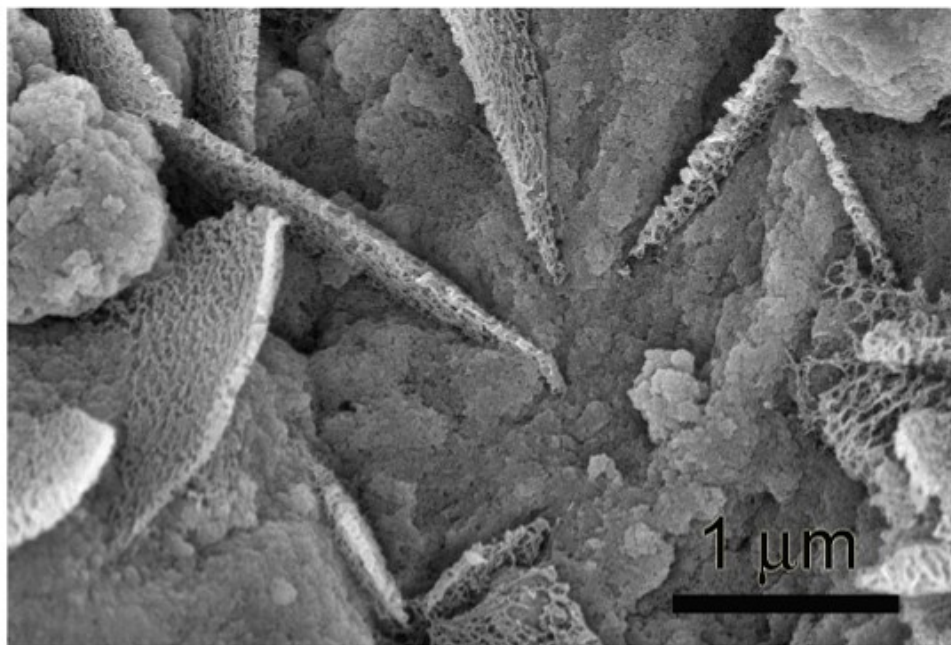Corresponding to: E-mail: xinhaoli@sjtu.edu.cn (X.-H. Li) chemcj@sjtu.edu.cn (J.-S. Chen)
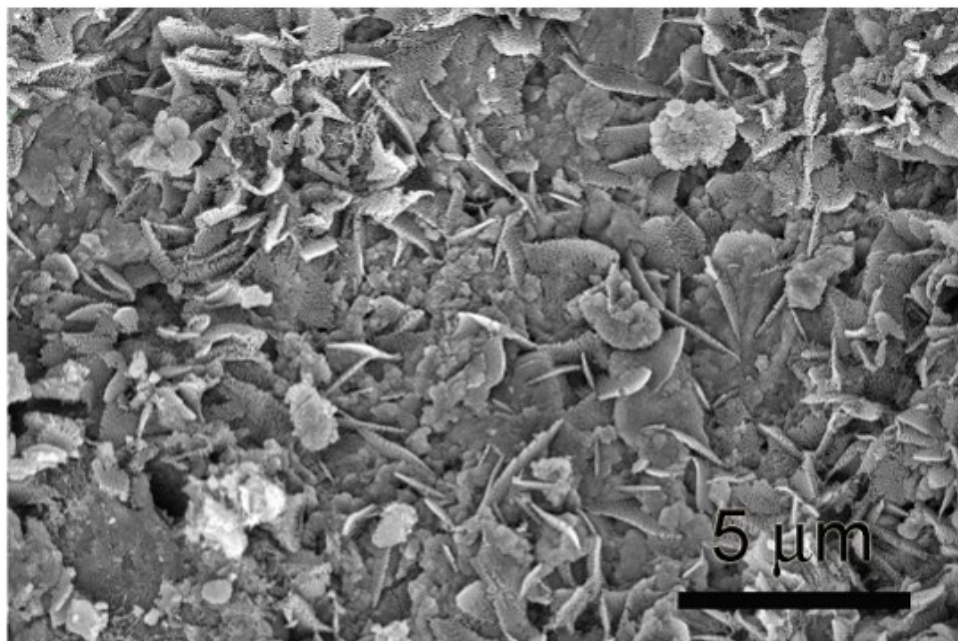
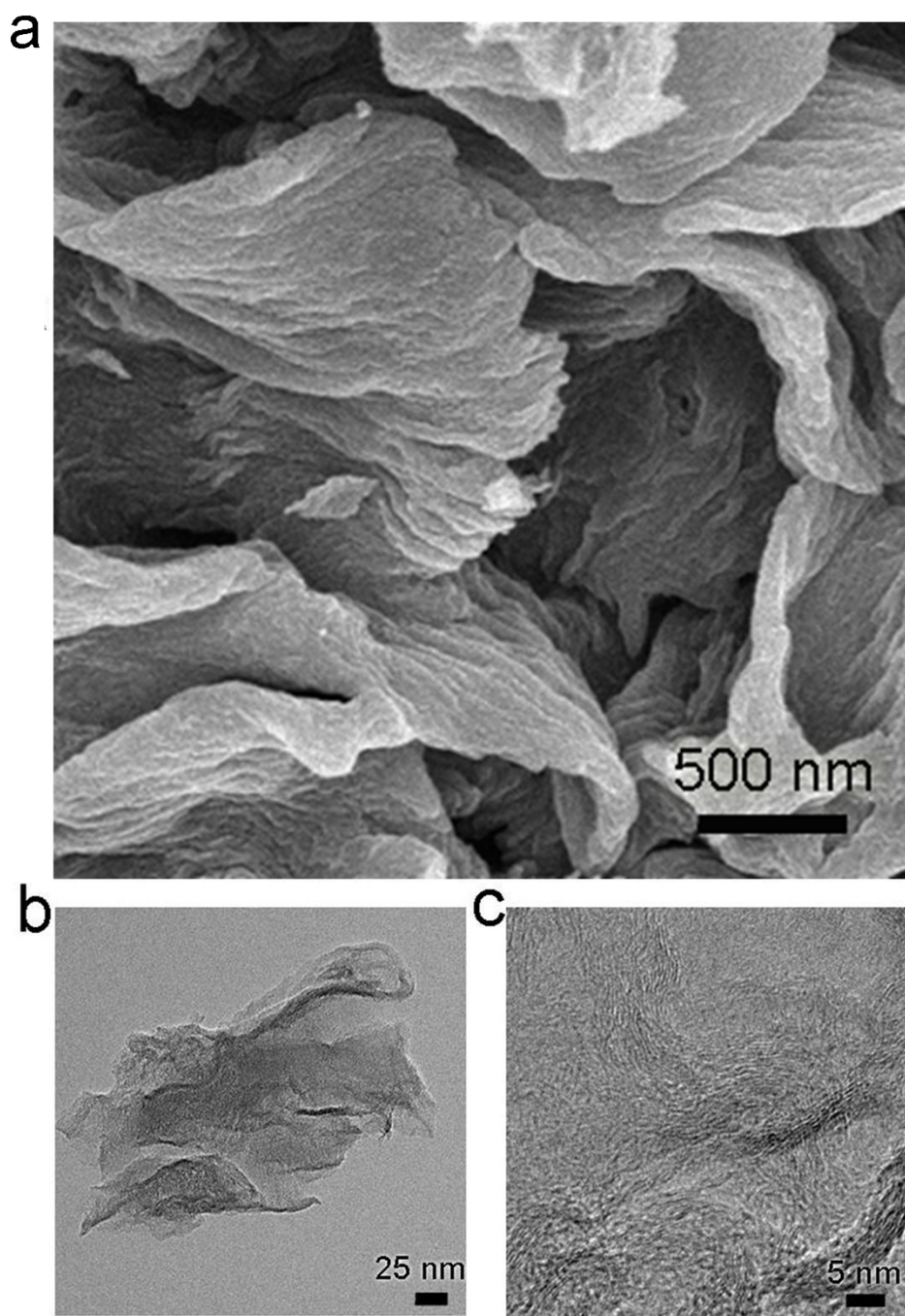**Figure S1.** SEM images of TiN/Cnet obtained at 1000 °C.

Figure S2. SEM images (a), TEM (b) and HRTEM (c) images of layered carbon obtained at 1000 °C.
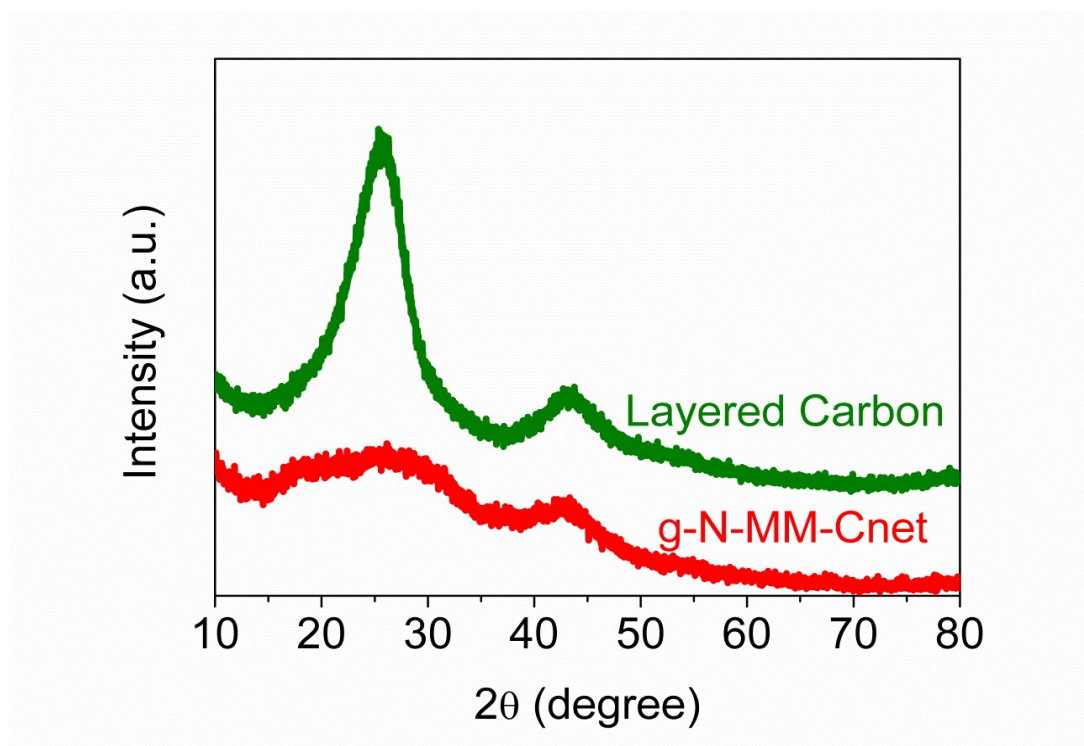
Figure S3. XRD patterns of g-N-MM-Cnet and layered carbon obtained at 1000 °C. The XRD patterns of g-N-MM-Cnet and layered carbon with typical peaks at 25.71 and 43.43 degrees matched well with the peaks of graphite (JPCDS: no. 65-6212).
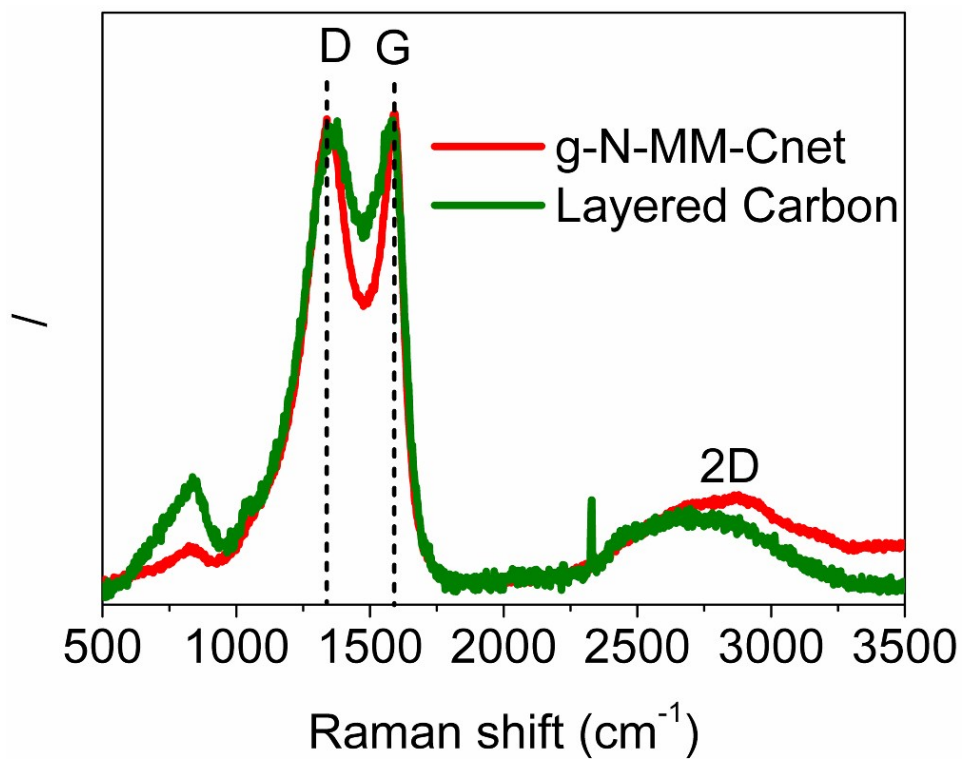
Figure S4. Raman spectrum of g-N-MM-Cnet and layered carbon. Typical Raman peaks of graphite lattice (G band) at 1575 cm^{-1} as well as the (weak) disorder band caused by the graphite edges (D band) at approximately 1355 cm^{-1} were also observed in our sample.
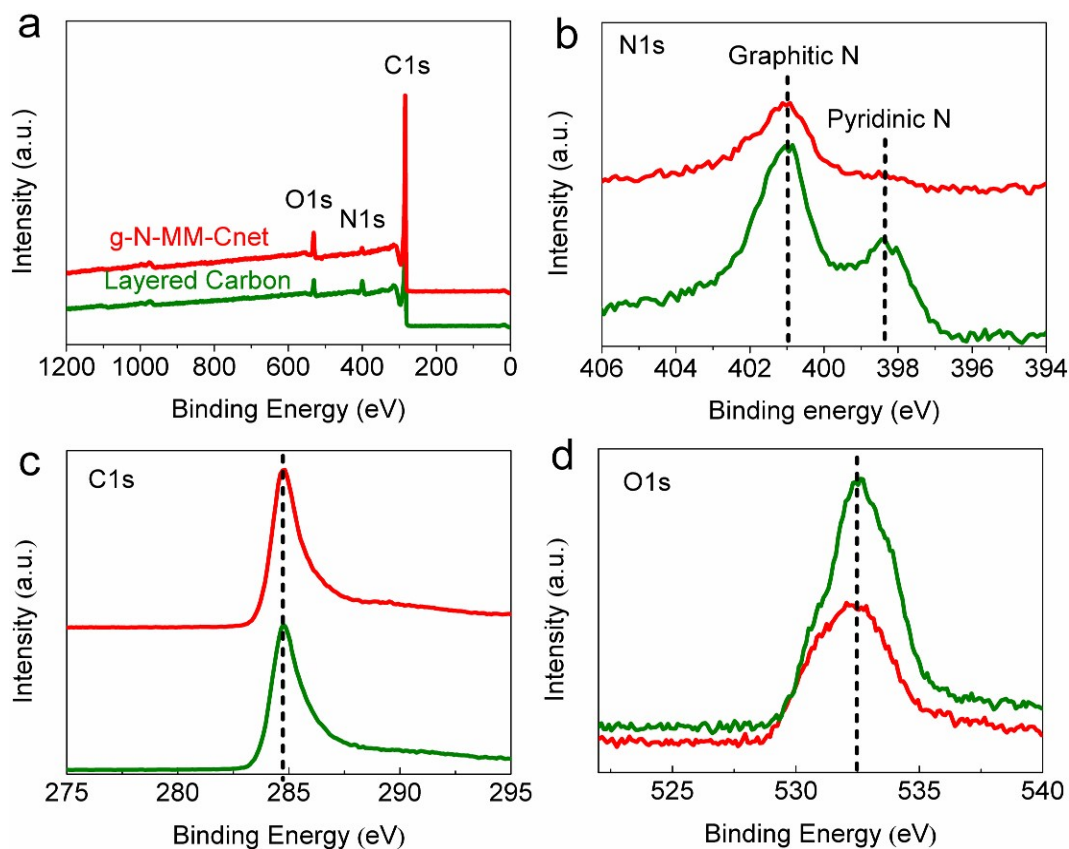
Figure S5. XPS survey spectrum (a) and high-resolution XPS N1s (b), C1s (c) and O1s (d) spectrum of g-N-MM-Cnet and layered carbon.

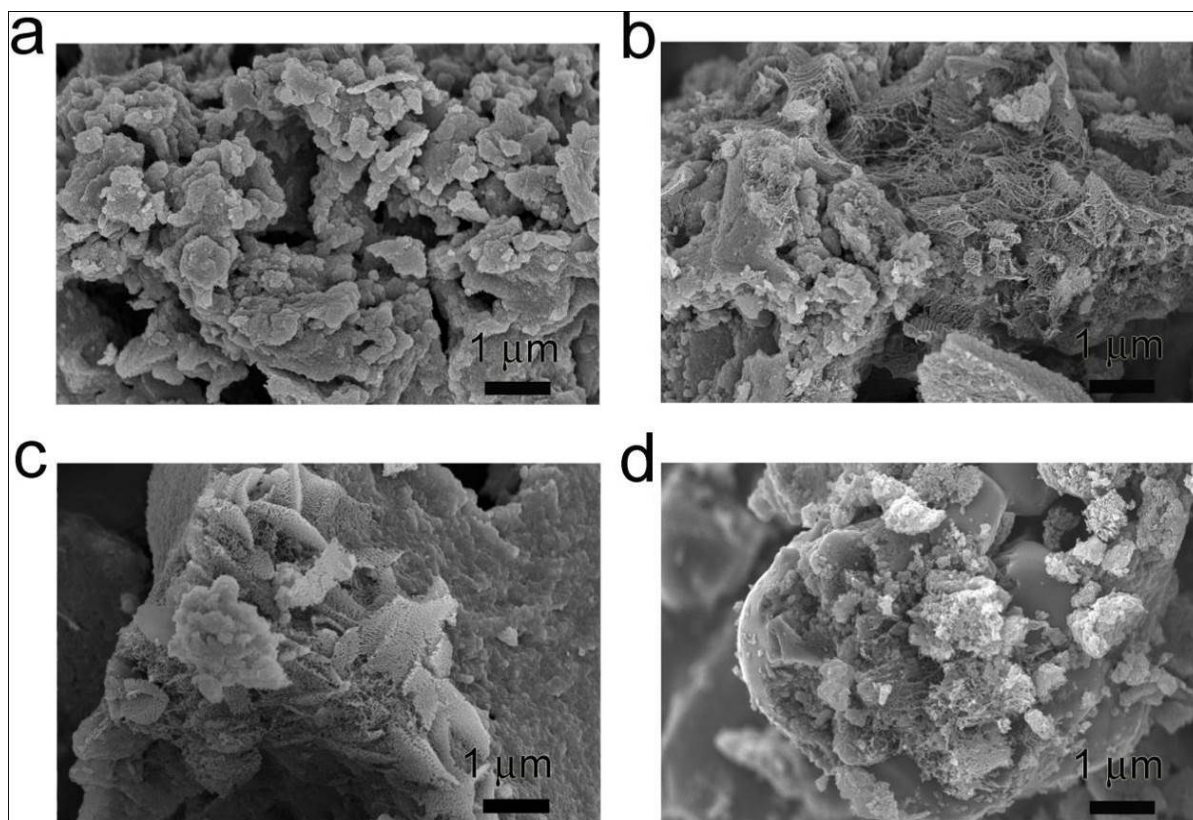**Figure S6.** SEM images of TiN/Cnet with different molar ratio of TTIP and P123: (a) 1:0, (b) 1:0.0068, (c) 1:0.0135, (d) 1:0.027, 800 °C, 1 h. Only irregular aggregates of nanoparticles were observed without the involvement of P123 (Figure S6a). Carbon nanonets formed only when P123 were added. All these results indicated the role of P123 as carbon source for the formation of carbon nanonets.
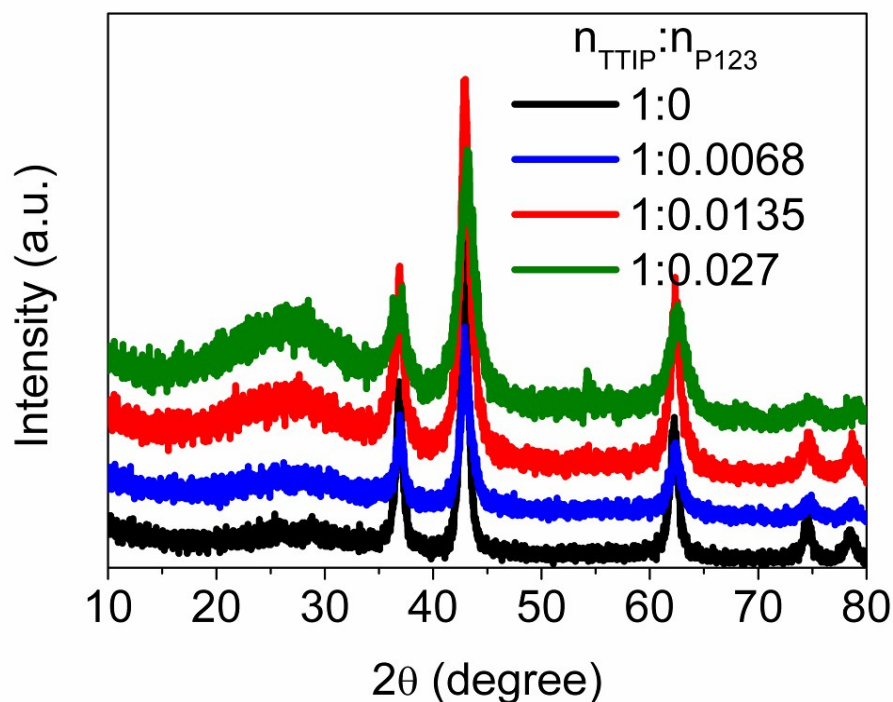
Figure S7. XRD patterns of TiN/Cnet samples obtained at 800 °C for 1 h with different molar ratios of TTIP and P123 (n_{TTIP} : n_{P123}): (a) 1:0, (b) 1:0.0068 , (c) 1:0.0135 , (d) 1:0.027. The peak around 26 degrees indicated the gradually increased content of graphite components in the samples with more and more P123 added. The TiN components exhibited the characteristic diffraction peaks of typical cubic phase TiN (NaCl-type structure, JCPDS No. 38-1420) at 36.91, 43.11, 62.61, 74.11 and 77.91 degrees, ascribed to the crystal planes of (111), (200), (220), (311) and (222), respectively. Without the addition of P123, no obvious signal of carbon components was detected in the XRD pattern of the control sample. The white color of such a control sample further unambiguously excluded the formation of carbon components.
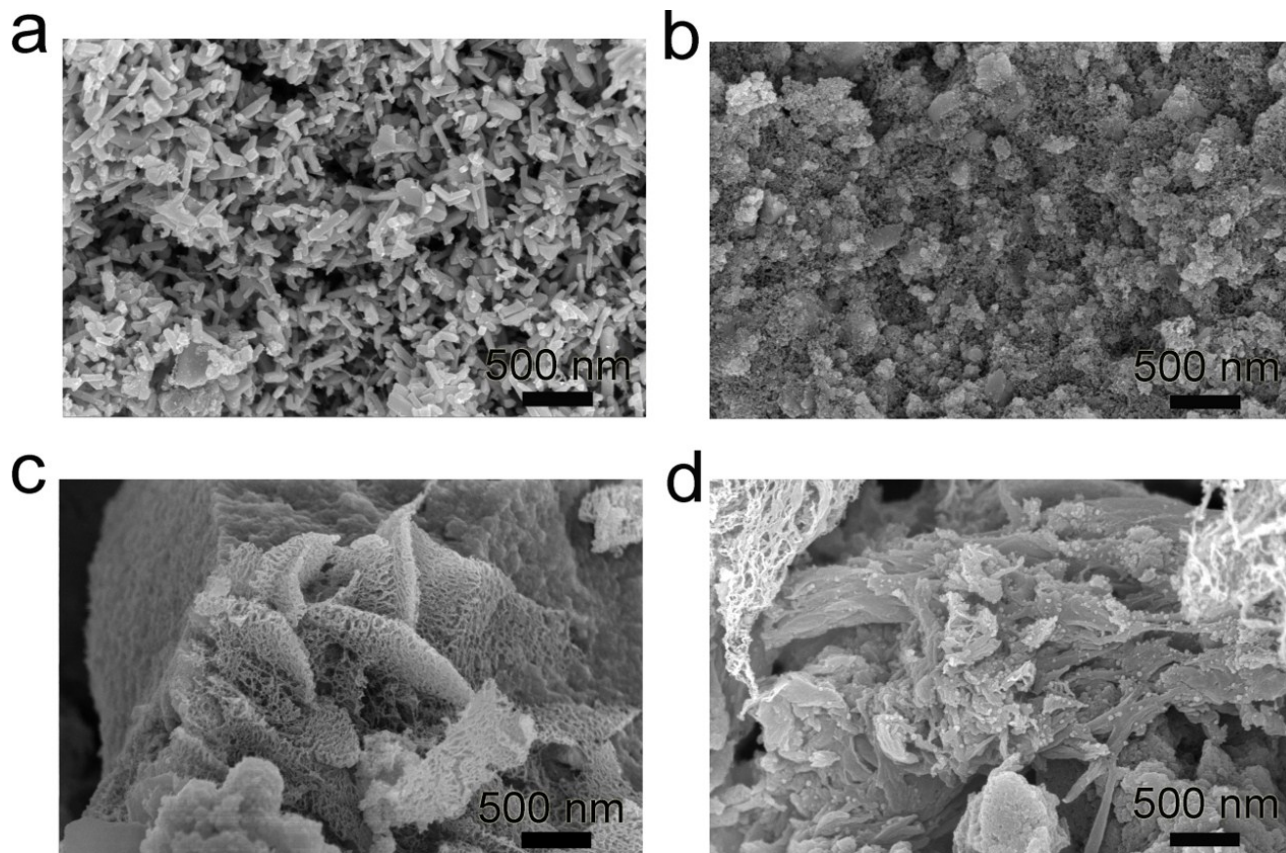
Figure S8. SEM images of TiO$_2$/Cnet with different molar ratios of TTIP and DCDA: (a) 1:0.6, (b) 1:1.2, SEM images of TiN/Cnet with different molar ratios of TTIP and DCDA: (c) 1:2.5, (d) 1:6, 800 °C, 1 h. The maximum molar ratio of TTIP and DCDA was optimized to be 1:1.2 (Figure S8b) to ensure the formation of Cnet. Even less DCDA added could only give the formation of bare TiO$_2$ nanoparticles (Figure S8a). The contribution of carbon atoms in DCDA to the yield of carbon was excluded as excess amount of DCDA could not lead to obvious increase in the amount of carbon nanonets (Figure S8d).
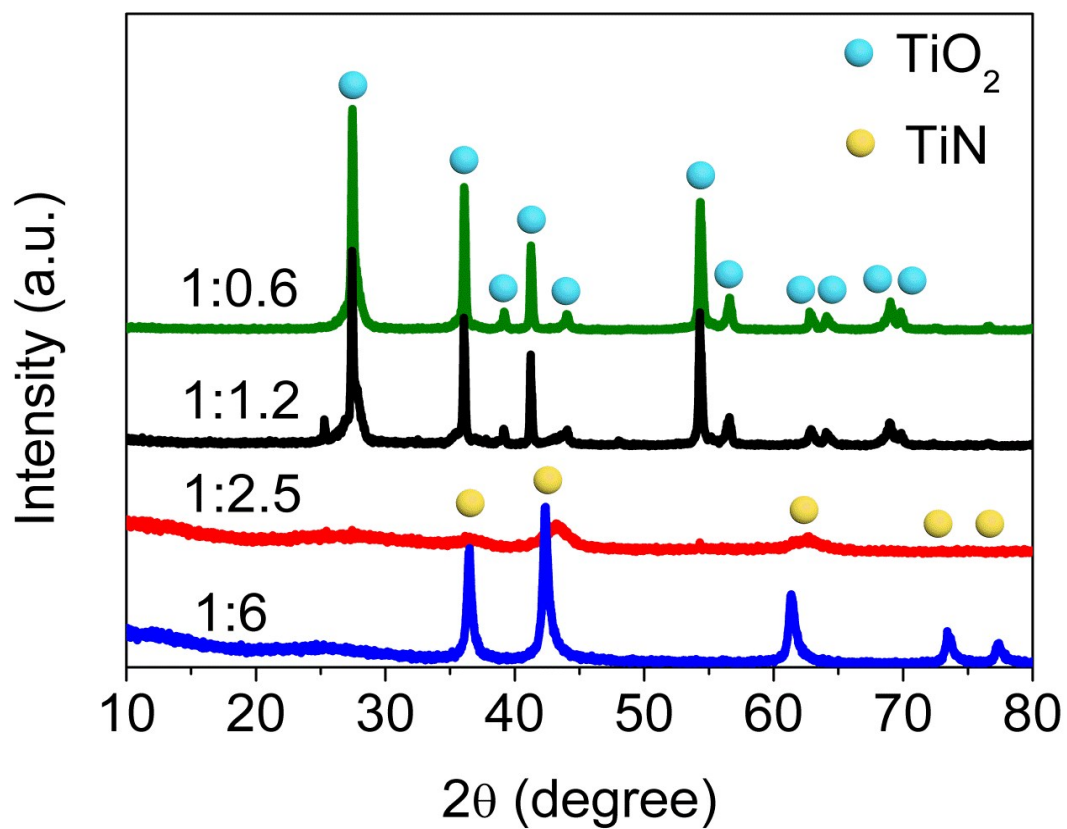
Figure S9. XRD patterns of TiN/Cnet with different molar ratios of TTIP and DCDA: (a) 1:0.6, (b) 1:1.2, (c) 1:2.5, (d) 1:6, 800 °C, 1 h. The content of TiN increased with more DCDA added, suggesting the role of DCDA as nitrogen source.
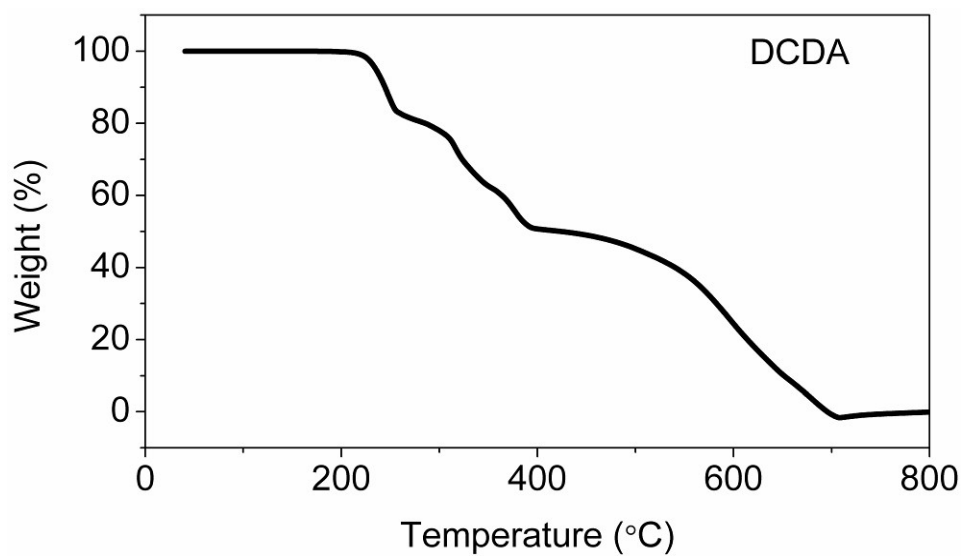
Figure S10. TGA analysis of the DCDA. The formation of carbon nitride at around 550 °C has been well demonstrated in our previous work (ref. 30). At a temperature higher than 700 °C, the solid compound decomposed completely with a residue weight to be 0 %.
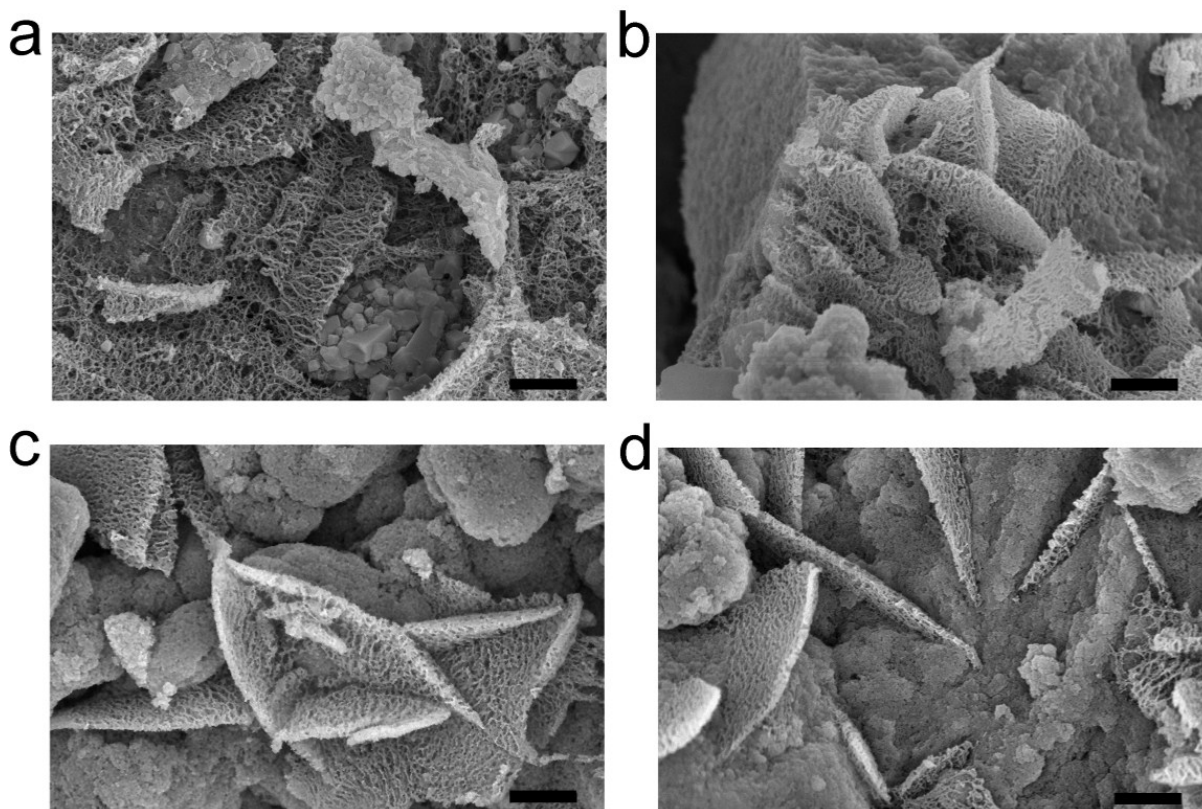
Figure S11. SEM images of TiO$_2$/Cnet (a) obtained at 600 °C and TiN/Cnet complexes obtained at 800 °C (b), 900 °C (c) and 1000 °C (d). Scale bar: 500 nm. The effect of TiN growth at elevated temperatures was however negligible on morphology of the carbon frameworks as revealed by the SEM observation.

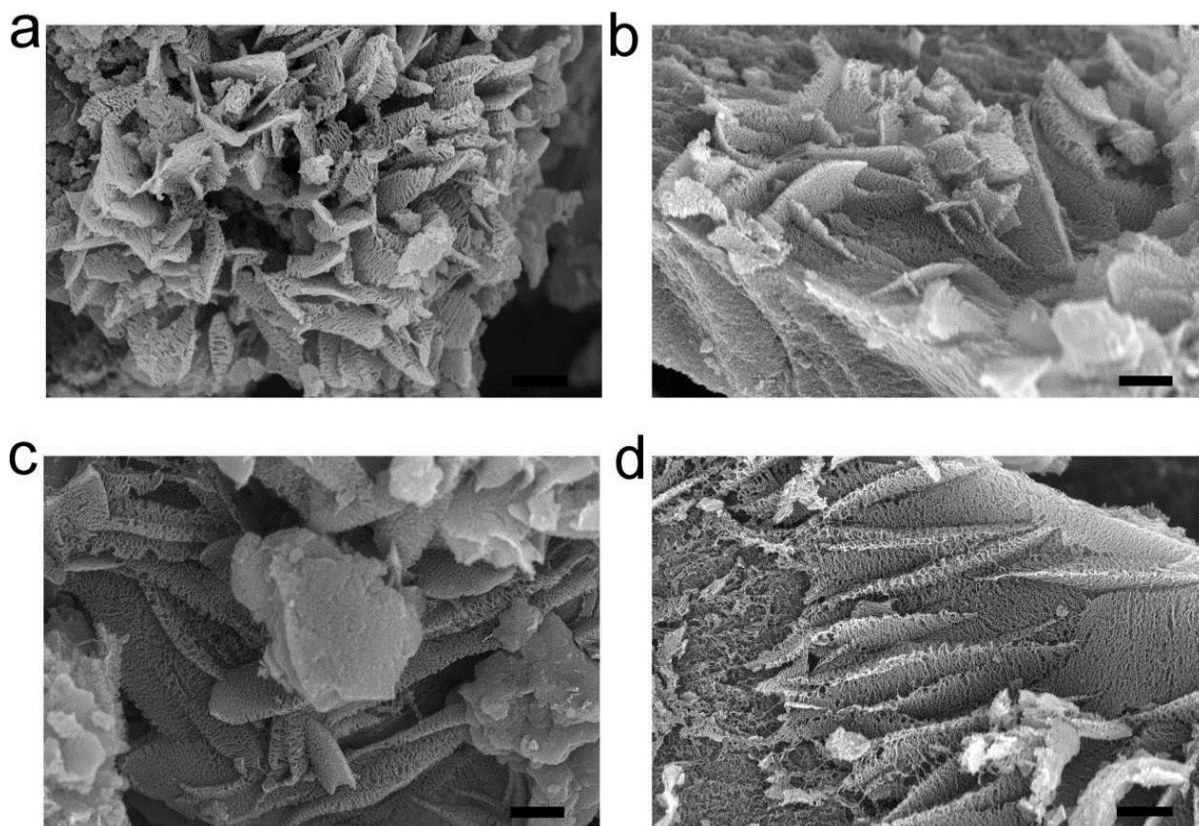**Figure S12.** SEM images of Cnet samples obtained at 600 °C (a), 800 °C (b) and 900 °C (c) and g-N-MM-Cnet (obtained at 1000 °C) after removal of TiO_2 or TiN templates. Scale bar: 1 μm. All the carbon sample were three-dimensional interconnected carbon networks as clearly seen in the amplified SEM images with nanoscale "net" holes. The morphology of carbon nets did not change significantly as elevating the annealing temperature.
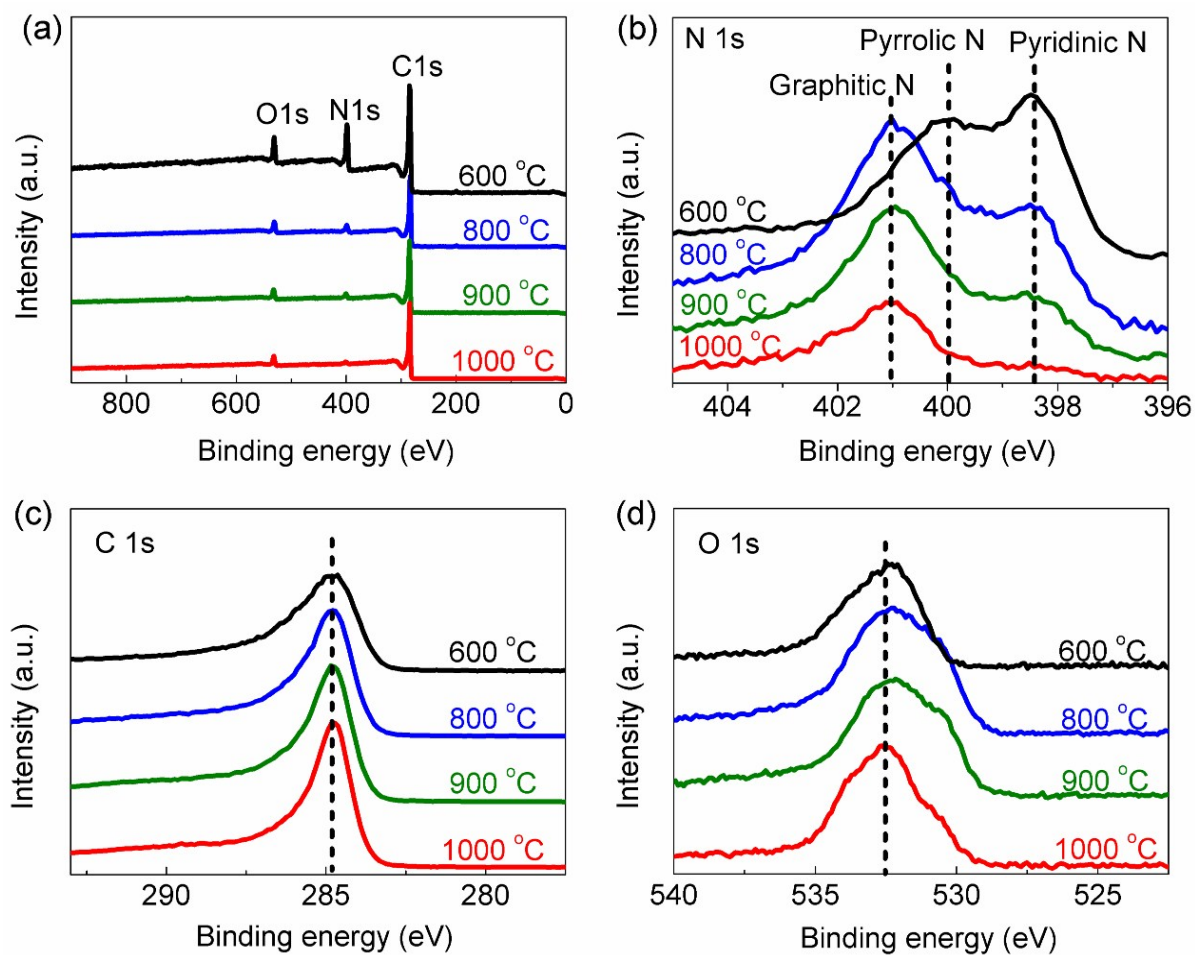
Figure S13. XPS survey spectrum (a) and high-resolution XPS N1s (b), C1s (c) and O1s (d) spectrum of g-N-MM-Cnet (obtained at 1000 °C) and Cnet samples obtained from 600 to 900 °C.
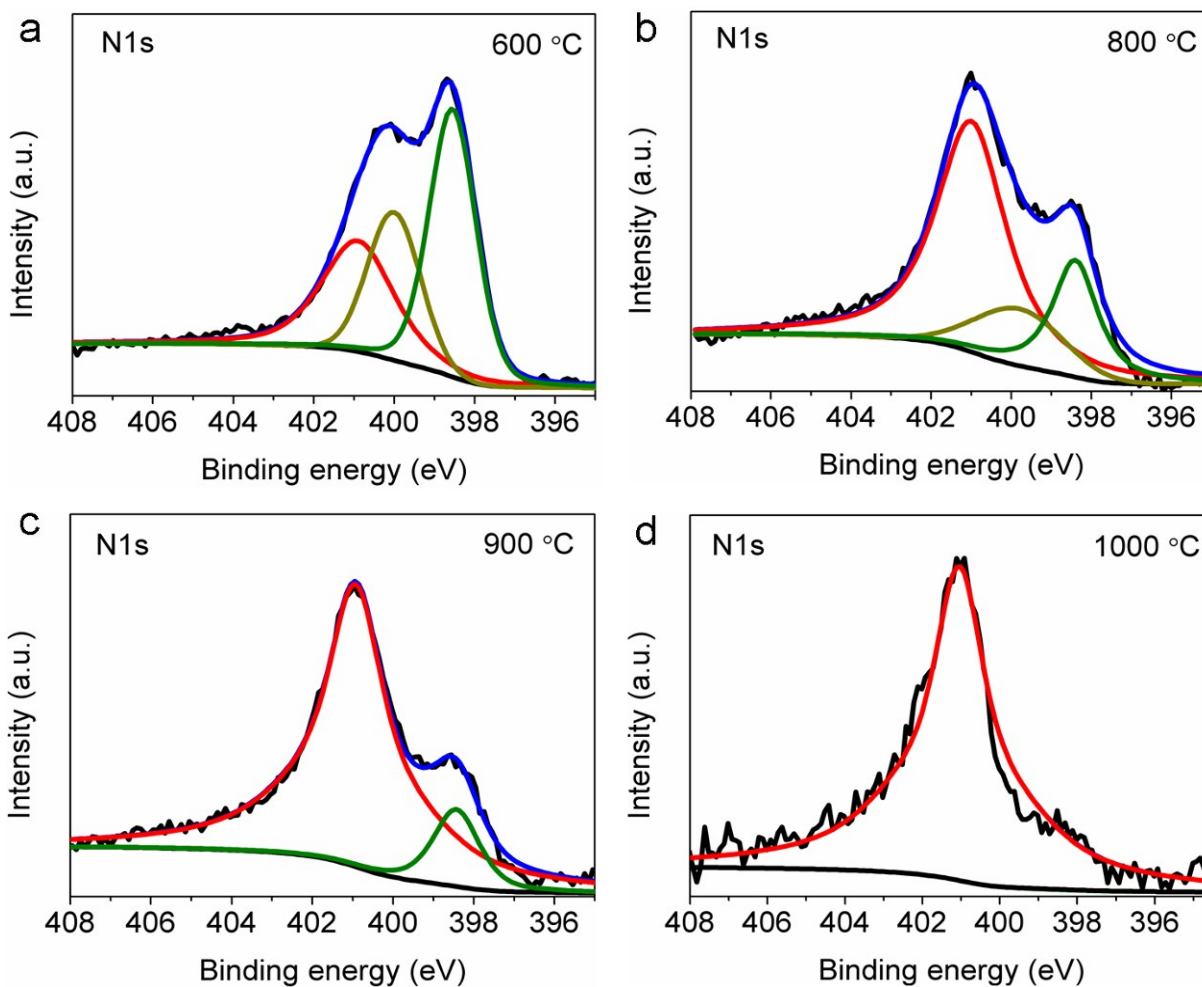
Figure S14. High-resolution XPS N1s spectrum of g-N-MM-Cnet (obtained at 1000 ℃) and Cnet samples obtained from 600 to 900 ℃.
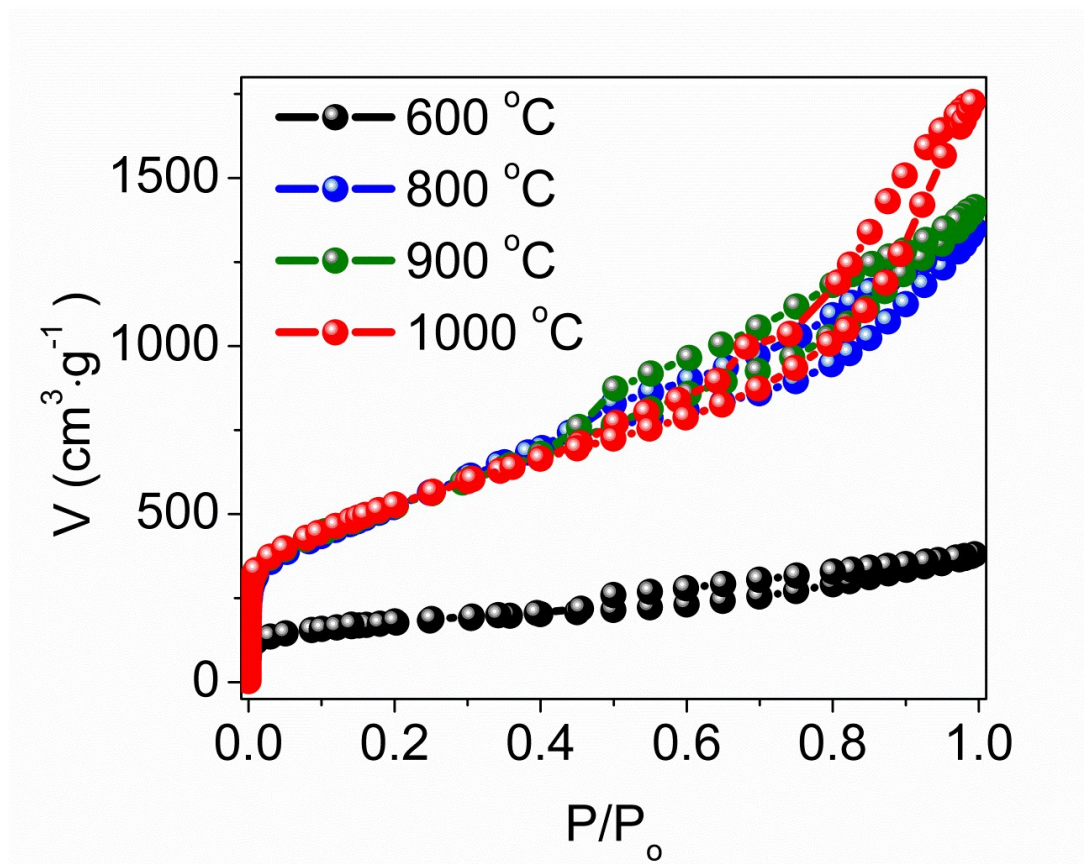
Figure S15. N_2 adsorption/desorption isotherms of g-N-MM-Cnet and control samples including Cnet-600 °C, Cnet-800 °C and Cnet-900 °C.
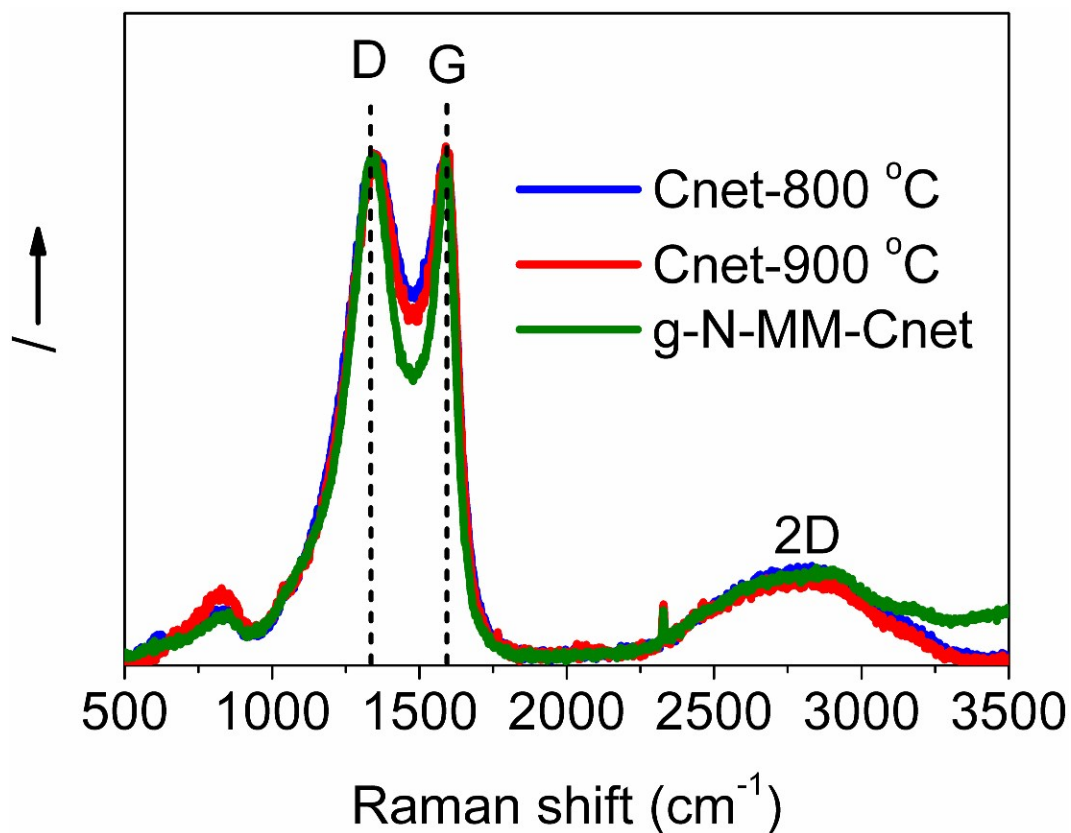
Figure S16. Raman spectrum of g-N-MM-Cnet and control samples including Cnet-800 °C and Cnet-900 °C. Typical Raman peaks of graphite lattice (G band) at 1575 cm^{-1} as well as the (weak) disorder band caused by the graphite edges (D band) at approximately 1355 cm^{-1} were also observed in control samples including Cnet-800 °C and Cnet-900 °C. The intensity ratio (I_D/I_G) of characteristic D and G bands in the Raman spectrum of carbon nanonet samples obtained at varied temperatures remained nearly the same. The reaction between nitrogen complexes and TiO$_2$ nanoparticles didn't disturb the graphite degree of Cnet samples obviously.

Figure S17. CV curves of g-N-MM-Cnet (a), layered carbon (b) and Pt/C (c) on RDE (catalyst loading: 0.1 mg·cm^{-2}) in O$_2$-saturated (solid line) and N$_2$-saturated (dash line) 0.1 M KOH at a scan rate of 10 mV·s^{-1}.
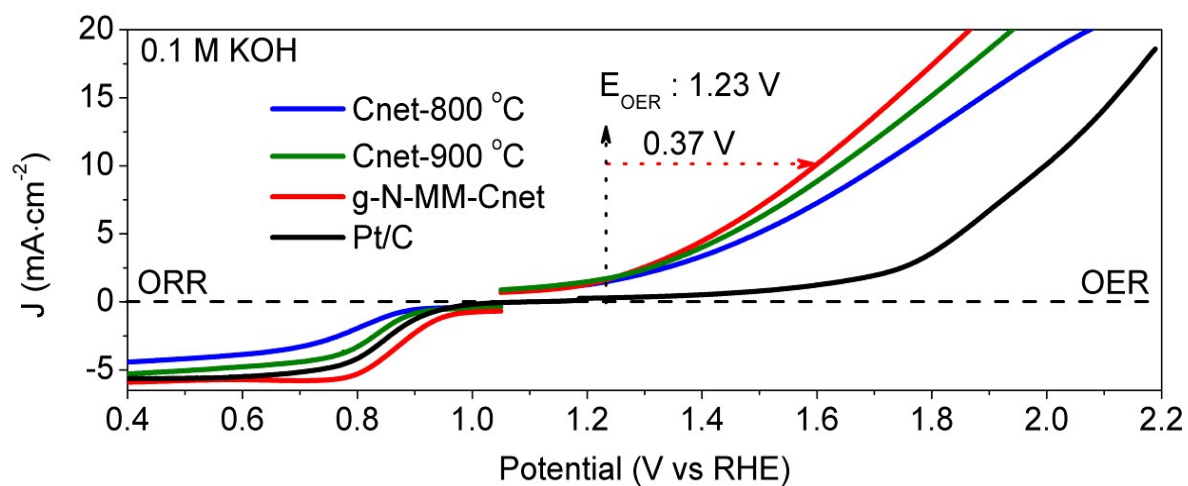
Figure S18. ORR and OER polarization curves of g-N-MM-Cnet, net-800 ℃, Cnet-900 ℃ and

Pt/C on RDE (catalyst loading: 0.1 mg·cm^{-2}) in 0.1 M KOH at a scan rate of 10 mV·s^{-1}.
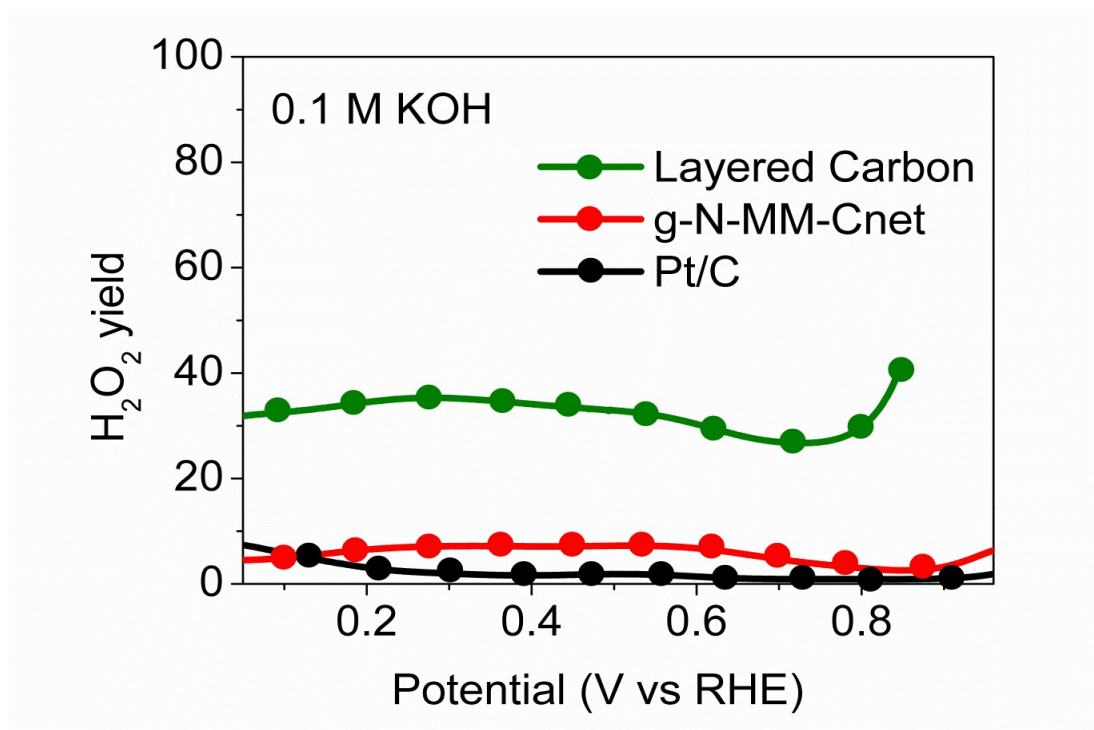
Figure S19. Hydrogen peroxide yields over layered carbon, g-N-MM-Cnet and Pt/C electrodes on RRDE for ORR in 0.1 M KOH. The H_2O_2 yield measured with g-N-MM-Cnet remains below 10 % at all potentials and drops to 2.5 % at about 0.85 V vs RHE, corresponding to a large number electrode transferred (3.95).
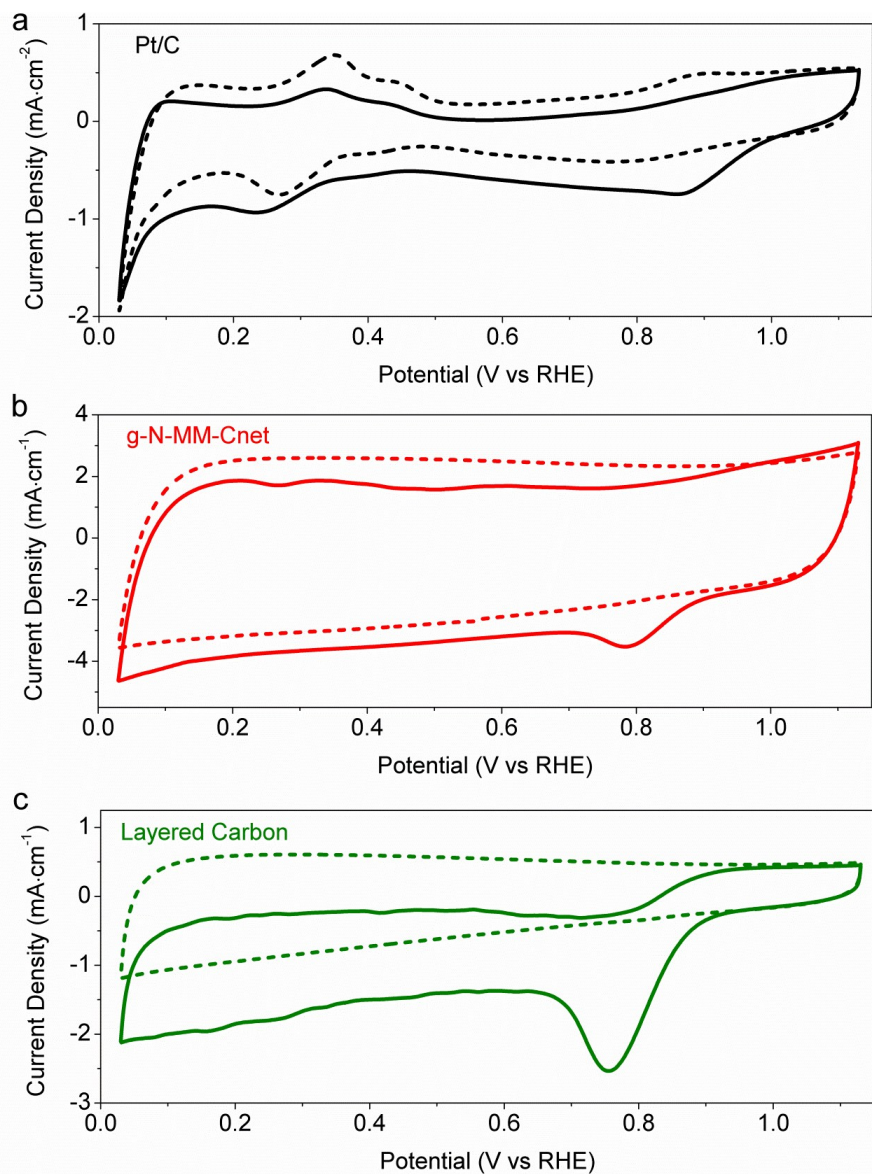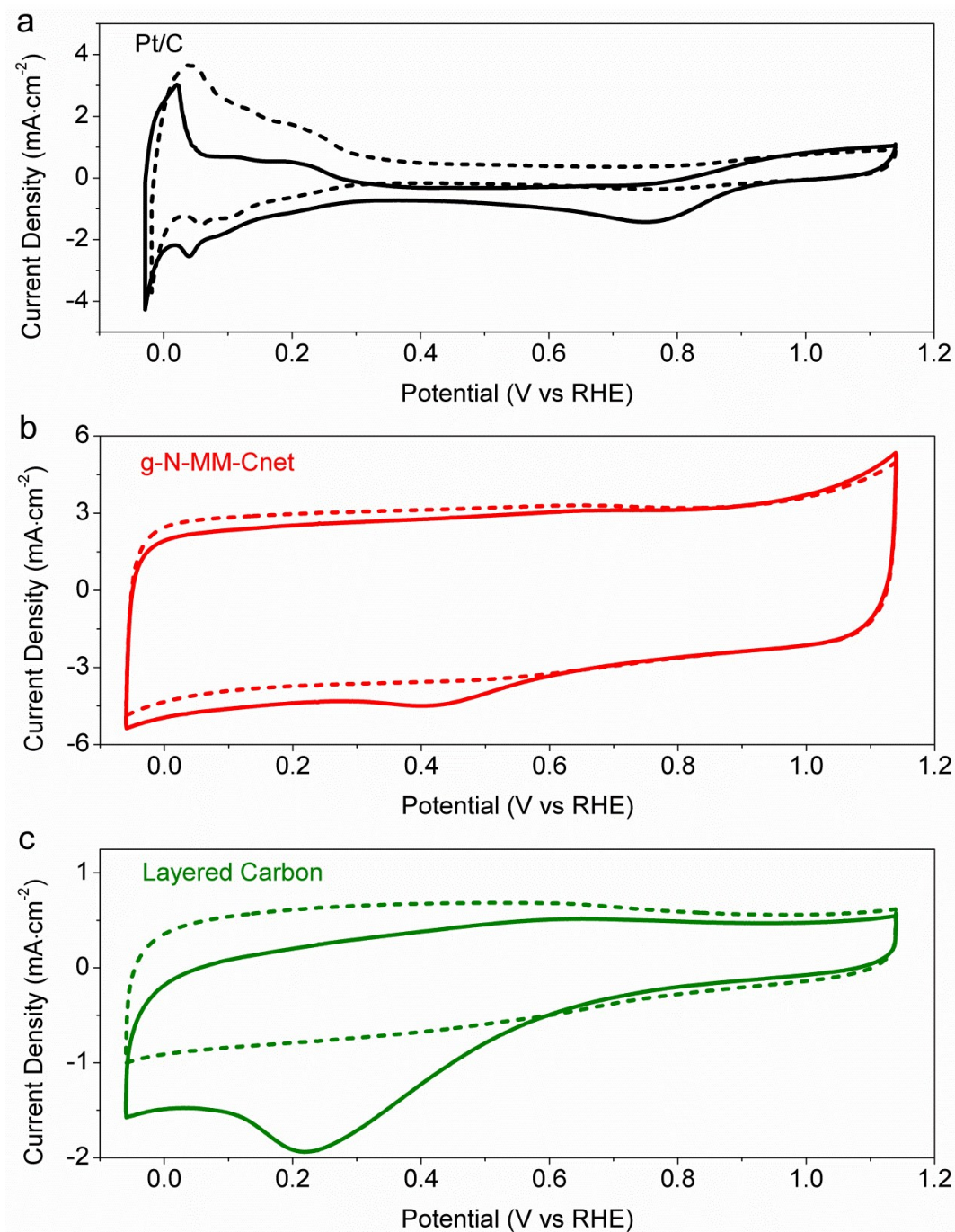
Figure S20. CV curves of g-N-MM-Cnet (a), layered carbon (b) and Pt/C (c) on RDE (catalyst loading: 0.1 mg·cm^{-2}) in O$_2$-saturated (solid line) and N$_2$-saturated (dash line) 0.5 M H$_2$SO$_4$ at a scan rate of 10 mV·s^{-1}. In contrast, for the electrolyte solution saturated with O$_2$, a pronounced redox response peak confirms electrocatalytic activity of all samples for oxygen reduction.
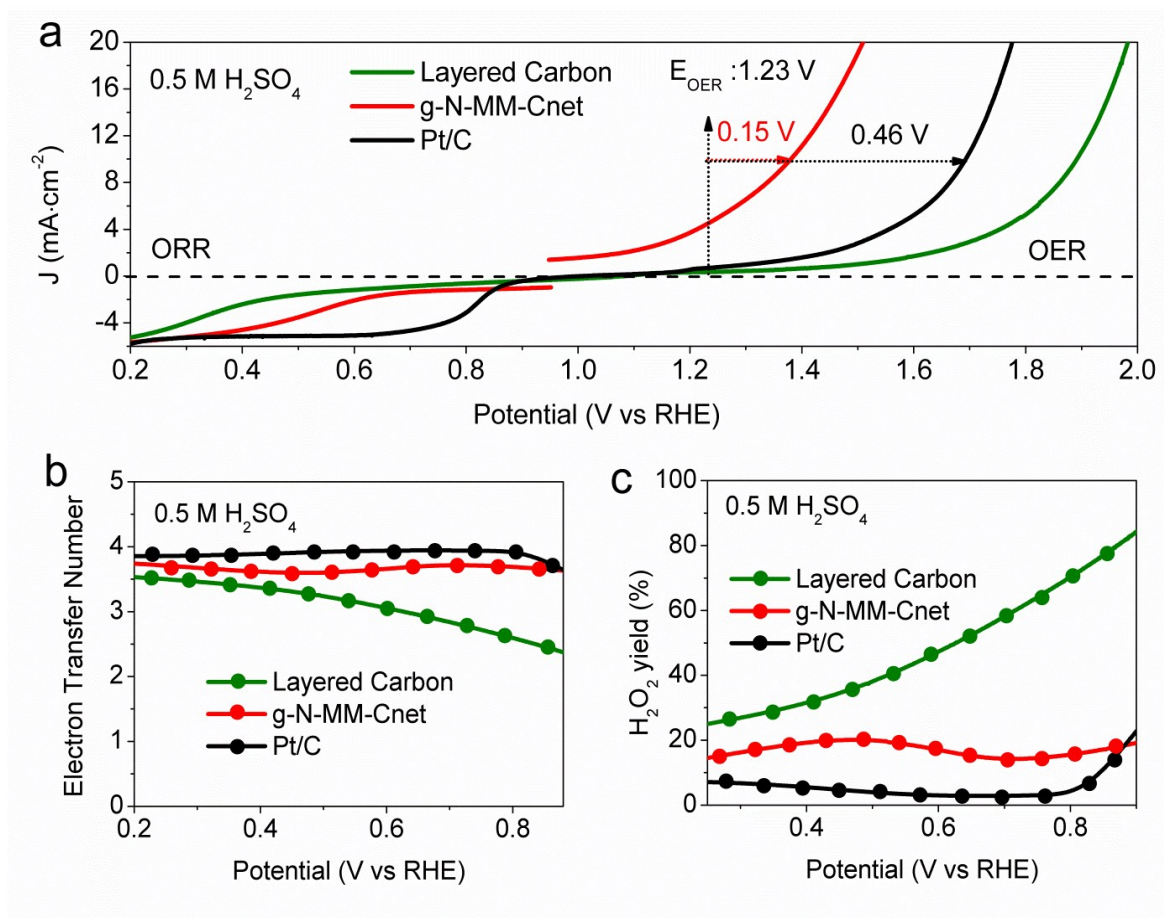
Figure S21. ORR and OER polarization curves (a) and the electron transfer numbers (b) for ORR of g-N-MM-Cnet, layered carbon and Pt/C on RDE (catalyst loading: 0.6 mg·cm^{-2}) in 0.5 M H$_2$SO$_4$, and corresponding hydrogen peroxide yields (c) tested over RRDE. The electron-transfer number values of g-N-MM-Cnet electrocatalyst were estimated to be 3.94-3.6 from 0.80 to 0.2 V versus RHE, suggesting a favorable 4e pathway of the ORR with water as the main product.
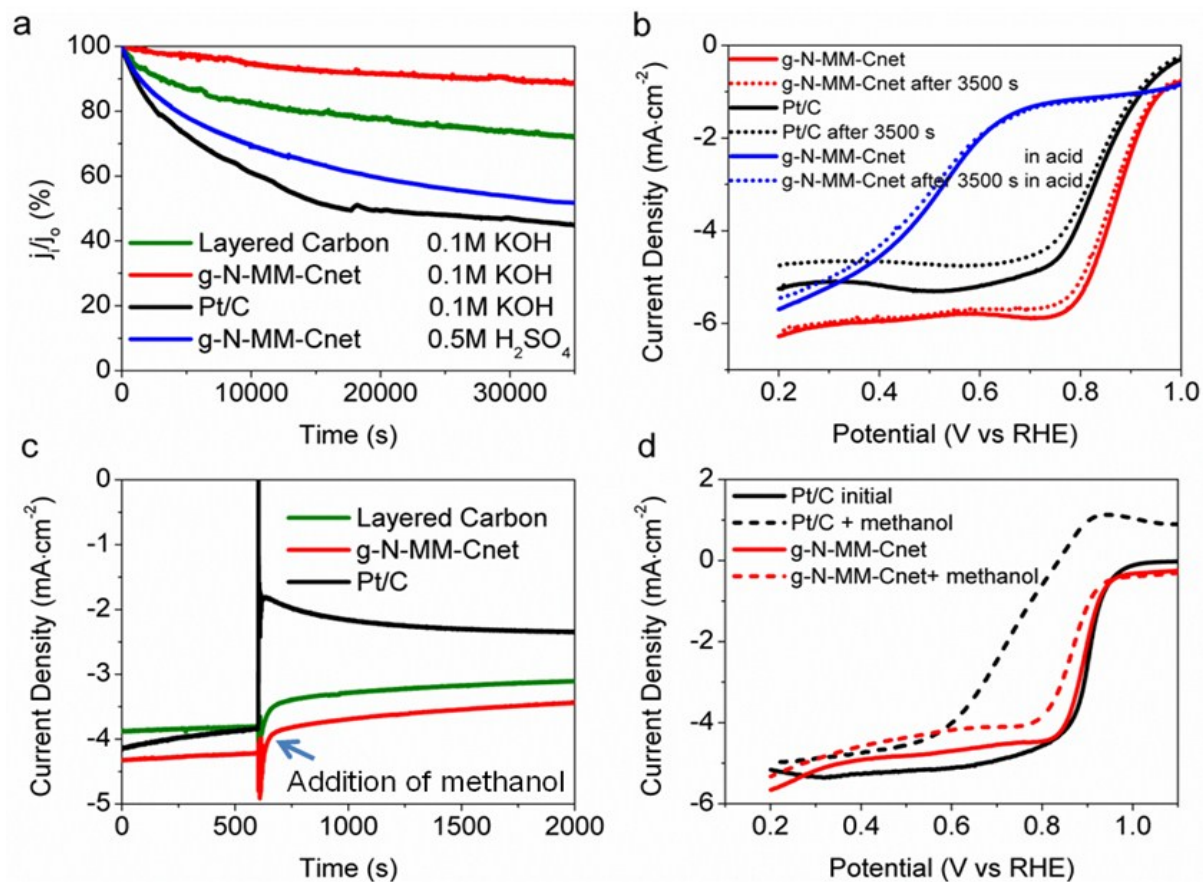
Figure S22. Chronoampero-metric responses (i-t) at 0.6 V vs. RHE (a), polarization curves before and after long-term tests (b), chronoamperometric responses (i-t) after addition of 3 M methanol (c) and polarization curves before and after addition of methanol for g-N-MM-Cnet, layered carbon and Pt/C samples tested in various electrolytes.
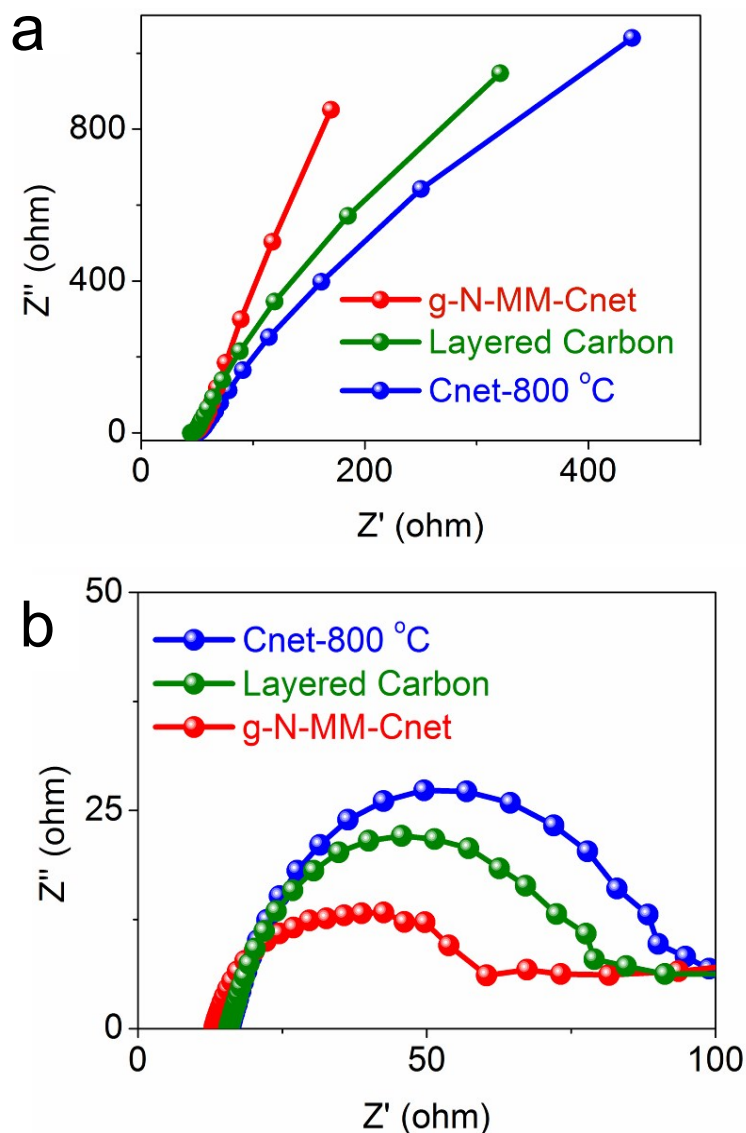
Figure S23. EIS spectrum of g-N-MM-Cnet, layered carbon or Cnet-800 °C samples. Catalyst ink made of carbon sample and Nafion solution was coated on a glassy carbon electrode (catalyst loading: 0.6 mg·cm^{-2}), which was further tested in O$_2$-saturated 0.1 M KOH at 0.85 V vs RHE with a 5 mV ac potential from 30 KHz to 0.1 Hz to get detailed diffusion behavior of the work electrodes (a). In order to test the real conductivity of these carbon samples, pure g-N-MM-Cnet, layered carbon or Cnet-800 °C samples were attached to foam Ni and used as work electrodes in a two-electrode system (b). For detailed methods used for EIS measurements, please see the experimental section of the supporting information.

Figure S24. TEM images of Ir/C used in this work. The mean diameter of Ir nanoparticles is around 4 nm.
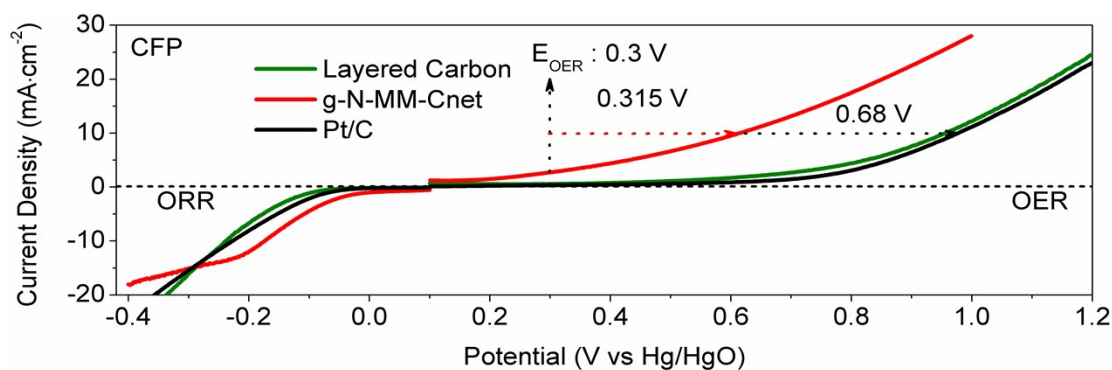
Figure S25. ORR and OER polarization curves of g-N-MM-Cnet, Ir/C and Pt/C on Teflon-coated carbon fiber paper (CFP) electrodes in 1 M KOH, respectively. The catalyst loading on CFP electrodes was 2 mg·cm^{-2} for all materials. On the catholic branch, g-N-MM-Cnet exhibited an ORR onset potential ∼ 39 mV positive than Pt/C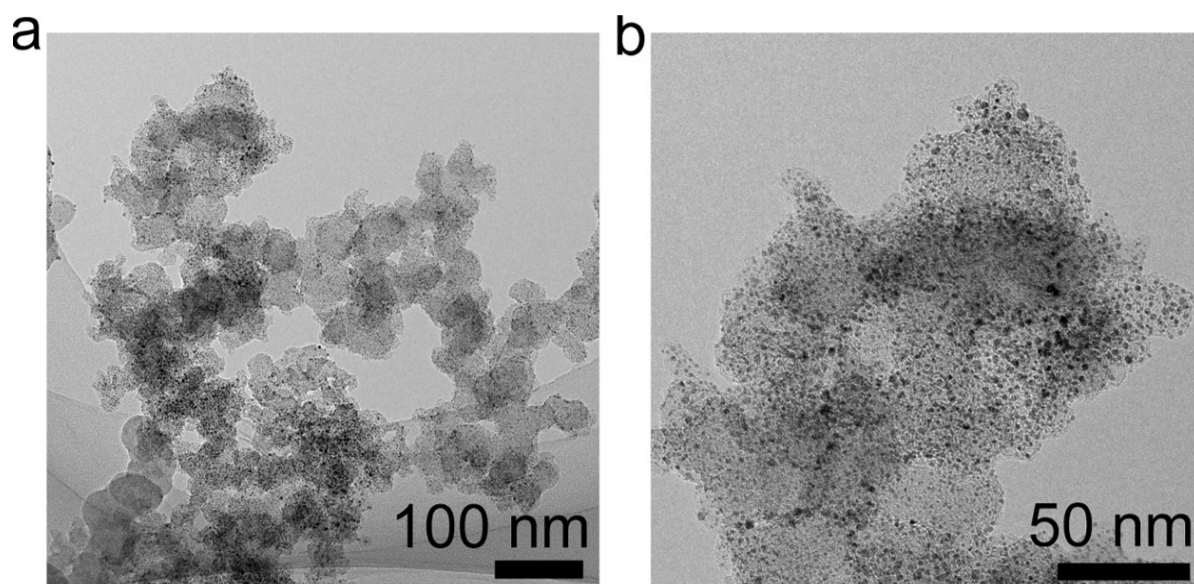. At a catholic current density of 10 mA·cm^{-2}, the g-N-MM-Cnet catalyst operated at 54 mV more positive potential than Pt/C. The g-N-MM-Cnet catalyst was also active for OER in the anodic potential regime, making it an appealing bi-functional catalyst in alkaline solutions. N doping carbon can supply the possible active sites for electrocatalyst. However, pyridinic N introduced into layered carbon and Cnets samples will inevitably lead to the formation of vacancy defects and thus hinders charge transfer, which is harmful to improve the activity of carbon electrocatalyst. Only graphitic nitrogen exists in g-N-MM-Cnet which could "activate" adjacent C atoms and simultaneously facilitate the electron transfer (Figure S25), resulting in much better ORR activity over g-N-MM-Cnet.
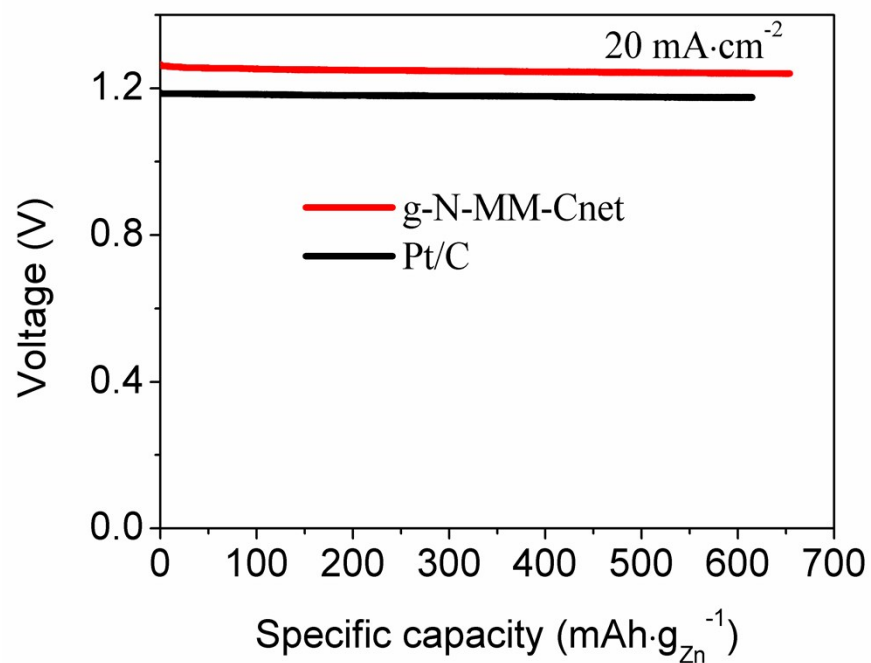
Figure S26. Long-time discharge curves of g-N-MM-Cnet and Pt/C based two-electrode Zn-air battery tested at 20 mA cm^{-2}, giving specific capacities of 653.7 and 614.8 mAh·Kg$_{Zn}^{-1}$, and corresponding energy density is 815.3 and 725.4 Wh·Kg$_{Zn}^{-1}$, respectively.
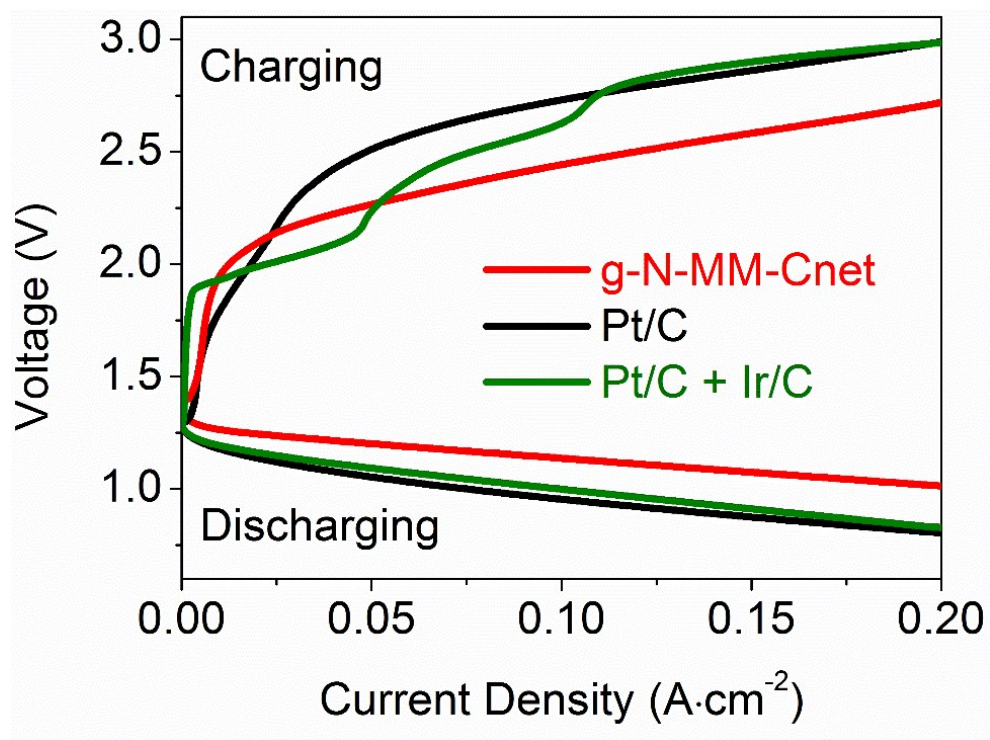
Figure S27. Charge and discharge polarization (V~i) curves of two-electrode Zn-air batteries made of g-N-MM-Cnet, Pt/C and Pt/C+Ir/C air cathodes.
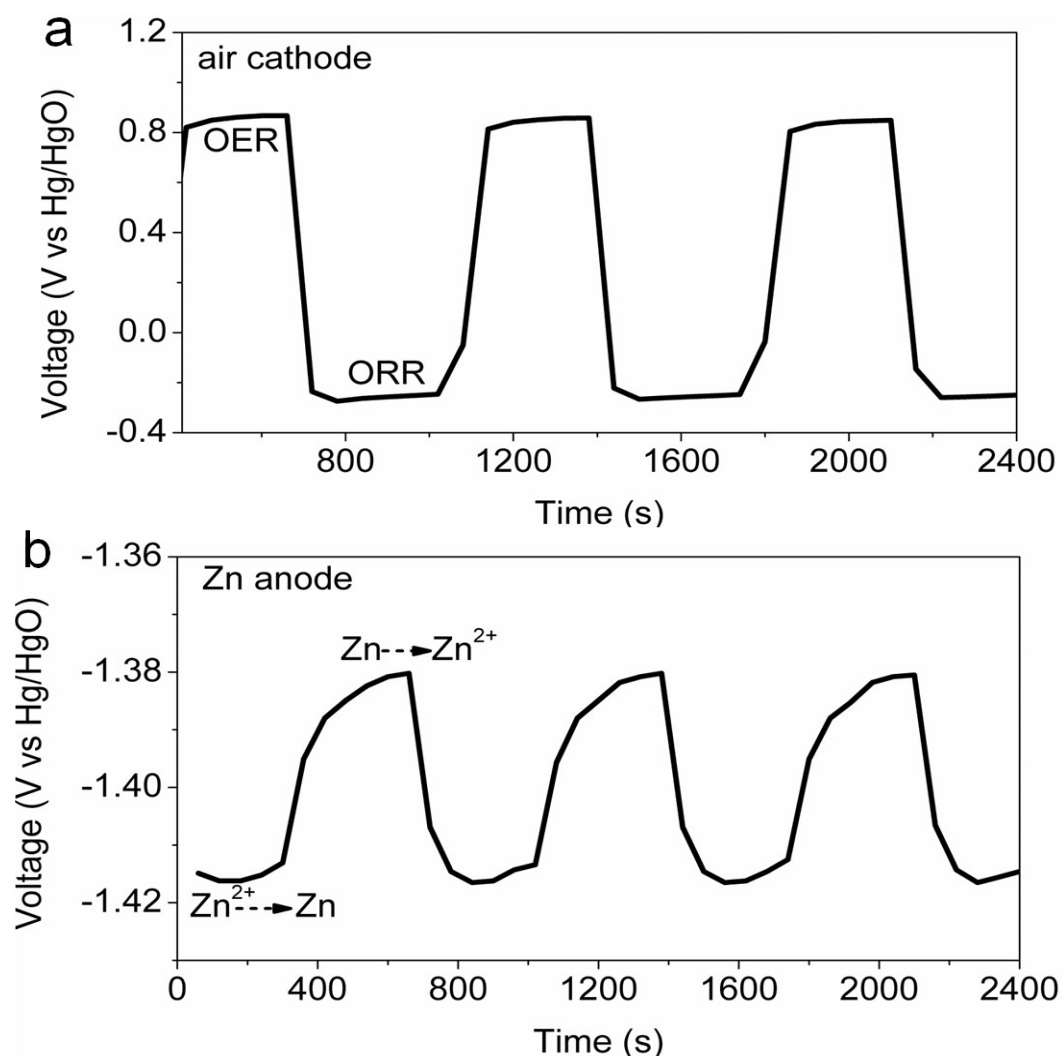
Figure S28. Alternating oxidation and reduction of (a) the air cathode and (b) the Zn anode at a current density of 10 mA·cm^{-2}. Based on above data, the voltage polarization was mainly contributed by the air cathode side (sum of ORR and OER overpotentials). Polarization (< 0.035 V) on the Zn anode was negligible.
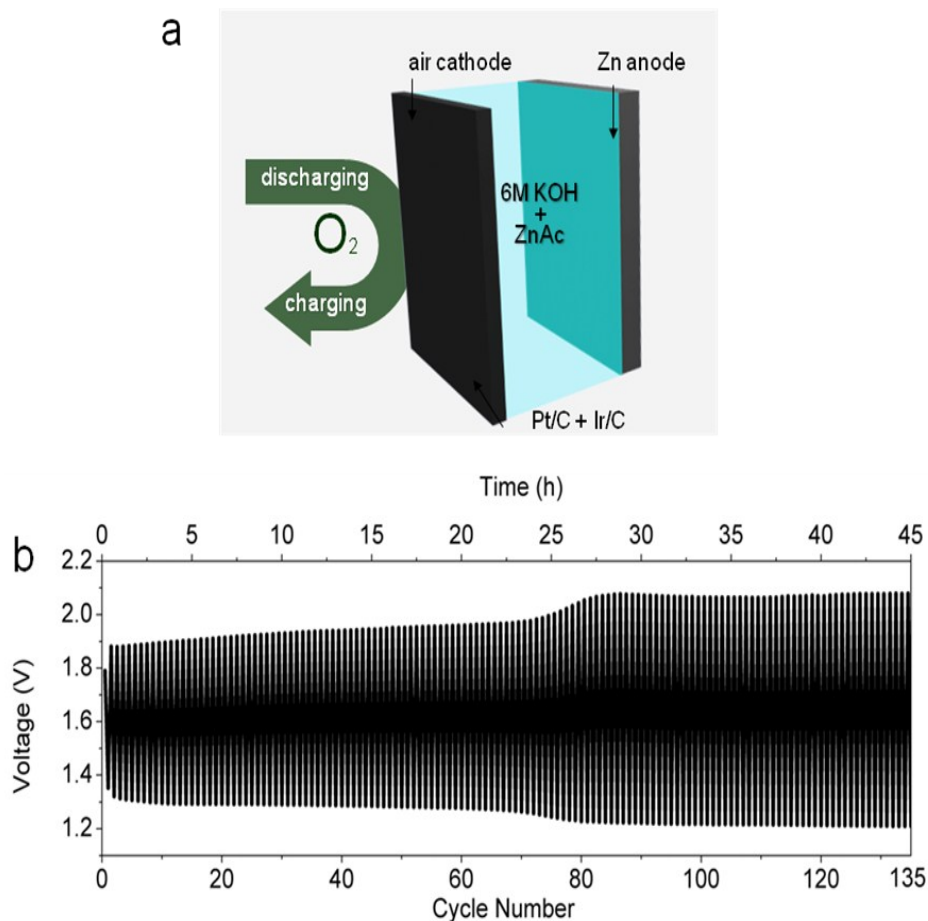
Figure S29. Schematic structure (a) and discharge/charge cycling curves (b) of two-electrode Zn-air batteries made of Pt/C+Ir/C air cathode. The mass ratio of Pt/C and Ir/C is 1:1 with a total loading of 2 mg·cm^{-2} on CFP. The as-formed Zn-air battery was run at 2 mA·cm^{-2} in a short cycle period (1200 s per cycle) in 6 M KOH. Although the charge-discharge voltage gap of Pt/C+Ir/C electrode was only 0.56 V at 2 mA cm^{-2}, slightly smaller than the voltage gap of the g-N-MM-Cnet electrode (0.8 V at the first cycle). The charge-discharge voltage gap of Pt/C+Ir/C electrode became broader after multiple charging-discharging cycles reached to 0.90 V after 80 cycles, suggesting the poor stability of air electrode based on Pt/C+Ir/C electrocatalyst.

Table S1. Synthesis conditions for layered carbon, g-N-MM-Cnet and control samples including Cnet-600 °C, Cnet-800 °C and Cnet-900 °C.

Sample	The molar ratios of TTIP/P123/HCl/H_2O/ethanol	DCDA	Temperature
Cnet-600 °C	1:0.0135:0.52:16:40	2.8 g	600 °C
Cnet-800 °C	1:0.0135:0.52:16:40	2.8 g	800 °C
Cnet-900 °C	1:0.0135:0.52:16:40	2.8 g	900 °C
g-N-MM-Cnet	1:0.0135:0.52:16:40	2.8 g	1000 °C
Layered Carbon	0:0.0135:0.52:16:40	2.8 g	1000 °C

Table S2. Bonding configurations for nitrogen atoms in N-doped carbon.
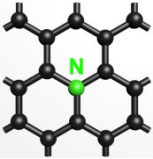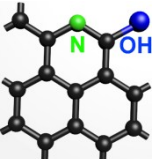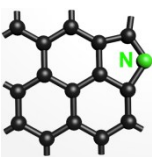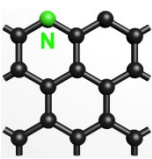
N species	Graphitic N	Pyridonic N	Pyrrolic N	Pyridinic N
XPS Binding Energy	401±0.1 eV	400.1±0.1 eV	399.9 ±0.1eV	398.5±0.1eV
Schematic structure				

Table S3. Surface area, pore width and volume of layered carbon, g-N-MM-Cnet and control samples including Cnet-600 °C, Cnet-800 °C and Cnet-900 °C, respectively.

Sample	BET Surface Area /m^2·g^{-1}	Total pore volume /cm^3·g^{-1}	Adsorption average pore width /nm	Mircopore width /nm	Mircopore pore volume /cm^3·g^{-1}
Cnet-600 °C	600.8	0.59	5.64	0.60	0.21
Cnet-800 °C	1843.3	2.09	4.38	0.64	0.55
Cnet-900 °C	1841.5	2.19	4.63	0.63	0.58
g-N-MM-Cnet	1947	2.67	5.66	0.64	0.58
Layered Carbon	106.8	0.47	17.42	--	0.03

All these parameters were calculated from N$_2$ adsorption/desorption analysis results.

Table S4. The atomic contents of C, N, O in layered carbon, g-N-MM-Cnet and control samples including Cnet-600 °C, Cnet-800 °C and Cnet-900 °C.

Sample	C /%	N /%	O /%
Cnet-600 °C	76.95	17.59	5.47
Cnet-800 °C	88.24	6.51	5.25
Cnet-900 °C	90.84	4.32	4.84
g-N-MM-Cnet	93.5	2.08	4.42
Layered Carbon	91.54	5.26	3.2

Table S5. The relative contents of graphitic N, pyrrolic N and pyridinic N in layered carbon, g-N-MM-Cnet and control samples including Cnet-600 °C, Cnet-800 °C and Cnet-900 °C respectively.

N species	Pyridinic N /%	pyrrolic N /%	Graphitic N /%
Cnet-600 °C	43.42	24.92	31.66
Cnet-800 °C	20.27	11.87	67.85
Cnet-900 °C	12.26	0	87.74
g-N-MM-Cnet	0	0	100
Layered Carbon	17.07	0	82.93

We use the XPSPEAK software to calculate the relative atomic percentage of pyridinic N and graphitic N from high-resolution XPS N1s spectrum of g-N-MM-Cnet and layered carbon obtained at 1000 °C. The dopant species of the nitrogen within the carbon net materials were observed to be dependent on the TiO_2 species. As shown in Table S5, the relative content of the graphite nitrogen species was 100 and 82.93 % in g-N-MM-Cnet and layered carbon respectively. This may be due to the fact that TiO_2 species as selective "absorber" of nitrogen atoms at the edge or defect cites to prepare graphitic nitrogen-doped nanocarbons. The dopant species of the nitrogen within the carbon net materials were observed to be dependent on the annealed temperature. As shown in Table S5 and Figure S12, the relative content of the graphite nitrogen species increases from 31.66 to 100 % with increasing annealed temperature, while the relative content of pyridinic nitrogen species correspondingly reduces from 43.42 to 0 %, the relative content of pyrrolic nitrogen species reduces from 24.92 to 0 %. This may be due to the fact that graphite-like nitrogen species own higher binding energy than pyridinic-like nitrogen species, and higher thermal stability is reasonably expected.

Table S6. Performance of g-N-MM-Cnet-based two-electrode Zn-air battery and state-of-the-art rechargeable Zn-air batteries in the literature.

Electrocatalysts	Zn electrode/ electrolyte	Current Density @ V = 1.0 V $(mA \cdot cm^{-2})$	Peak power density $(mA \cdot cm^{-2})$	Specific capacity $(Wh \cdot Kg_{Zn}^{-1})$	Ref.
g-N-MM-Cnet	Zn plate/6M KOH	210.5	560	866.4	This work
NPMC-1000	Zn plate/6M KOH	< 30	~70	~835	6
N, B doped CNT	Zn plate/6M KOH	< 20	~50	—	S1
Porous N doped graphene	Zn foil/6M KOH	~70	~100	—	S2
CoO/N-CNT	Zn foil/6M KOH	197	~265	>700	13
Meso/micro-PoPD	Zn foil/6 M KOH	—	—	800	7
CuPt-NC	Zn foil/6 M KOH	188.8	253.8	728	15
Mn₃O₄/graphene	Zn powder/6M KOH	70	~175	—	S3
Amorphous MnOₓ/C	Zn powder/6M KOH	120	~250	< 320	S4
FeCo-EDA	Zn plate/6M KOH	150	~360	—	S5

Table S7. Rechargeability of g-N-MM-Cnet-based two-electrode Zn-air battery and state-of-the-art rechargeable Zn-air batteries in the literature.

Electrocatalysts	Configuration	Recharge-ability	Ref.
g-N-MM-Cnet	2-electrode	1200 s/cycle for 1464 cycles (488 h)	This work
NPMC-1000	2-electrode	600 s/cycle for 180 cycles (30 h)	6
NPMC-1000	3-electrode	600 s/cycle for 600 cycles (100 h)	6
N, B doped CNT	2-electrode	600 s/cycle for 80 cycles (~13.3 h)	S1
CoO/N-CNT	3-electrode	4-20 h/cycle for >200 h	13

References